IOP Publishing Physica Scripta
Phys. Scr. 95 (2020) 065502 (15pp) https://doi.org/10.1088/1402-4896/ab7ebb

3D non-paraxial kernel for two-point correlation modelling in optical and quantum interference at the micro and nano-scales

Román Castañeda, Jaime Moreno, Daniel Colorado and Julián Laverde

Physics School, Universidad Nacional de Colombia Sede Medellín, A.A. 3840 Medellín, Colombia

E-mail: rcastane@unal.edu.co

Received 23 November 2019, revised 2 March 2020
Accepted for publication 11 March 2020
Published 2 April 2020

Abstract

Optical and quantum interference at the micro and nano-scales are of growing interest. Its accurate description bases on the non-paraxial propagation of the spatial correlation, in which the physical observable, determined by the square modulus of the optical and quantum wave functions, is expressed as a modal expansion on a 3D non-paraxial geometric kernel, with the spatial correlation as coefficient. The kernel plays the main role of the model and is deduced from the optical wave equation in free-space as well as from the Schrödinger equation for particle propagation in field-free regions. Two features are analyzed in detail, i.e. the physical implications on the wave and particle interference due to the 3D spatial modulations provided by the local and non-local components of the kernel at the micro and nano-scales, and the decay of the kernel terms with the propagation distance which leads to a novel criterion for the kernel accuracy. The interference modeling is implemented on a matrix algorithm and is illustrated by some examples with nano-structured masks.

Keywords: optical interference, quantum interference, non-paraxial kernel, spatial correlation, micro-scale, nano-scale

(Some figures may appear in colour only in the online journal)

1. Introduction

Devices at micro and nano-scales are currently developed in optical and quantum technology. At these scales, non-paraxial propagation of waves and particles as well as effects due to the two-point correlation are unavoidable. The non-paraxial description is required because of the short propagation distances, significantly shorter than the limit distance that assures the validity of the paraxial approach. Two-point correlation effects appear because of the spatial coherence length, whose shortest value is of the order of the wavelength [1]. Furthermore, it has been shown that the interference modulation due to two-point correlation disappears for pairs of points with separation shorter than $\lambda/10$ [2].

The theory of optical coherence [1] concerns the two-point correlation in optical interference but, in spite of its general formulation, it is usually applied under paraxial approach [1] which is not applicable at micro and nano-scales. The standard description of quantum interference does not take into account explicitly the two-point correlation of the quantum wave function and its non-paraxial propagation at such scales [3]. The use of the paraxial approach in the standard description, for instance in the Feynman's path integral method [4], is presumably justified by the very short de Broglie wavelengths. Indeed, interference devices at the pico-scale, where the non-paraxial description is required, are not yet achievable by the current technology. However, the progress tendency is characterized by the attempts to develop technology at the molecular and atomic scales, for instance in electron nanoscopy for imaging biological nano-samples [5], which supports the relevance of a non-paraxial model to predict quantum particle interference. In addition, the rigorous modeling of the particle path along the first wavelengths

just after crossing the interference mask [6–9] requires a non-paraxial model.

It should be underlined that the modeling of the two-point correlation includes the propagation of the physical observable, determined by the square modulus of both the optical and quantum wave functions, as a component of the two-point correlation function [1, 4]. Thus, the two-point correlation accurately leads to the modeling of the energy distribution of optical interference patterns as well as the probability density function that predicts the built up of single particle interference patterns.

In spite of the above reasons, to implement the non-paraxial interference modeling under arbitrary spatial correlation is mathematically hard challenging, because the physical observables are expressed in terms of multi-dimensional modal expansions, whose kernel is complex valued and has Lorentzian shaped amplitude and non-linear argument. This complexity is an unavoidable accuracy requirement at the micro and nano-scales, that makes unsuitable the customary paraxial approached optical and quantum models. In addition, the local and non-local kernel features have physical implications on the spatial behavior of the optical waves and quantum particles in the setup volume, that the paraxial approached models cannot account for.

The aim of this paper is to discuss the spatially correlated non-paraxial modeling of both optical and quantum interference at the micro and nano-scales. To this aim, the same 3D non-paraxial, scalar, geometric and deterministic kernel is obtained by solving, by the Green's function method, the Helmholtz equation corresponding to the (time-independent) spatial component of the optical wave equation for free-space as well as of the Schrödinger equation for field-free particle propagation. This kernel is defined in the volume delimited by the input and output planes of the interference setup, and its mathematical features and physical implications are analyzed in detail.

The fundamentals of the 3D non-paraxial kernel deduction are summarized in section 2. The importance of the non-locality represented by the two-point correlation in optical and quantum interference is discussed in section 3, and the accuracy of the kernel is discussed in section 4. Some illustrative examples are shown in section 5, which were simulated by means of a recently reported matrix algorithm [10], and the conclusions are in section 6.

2. Fundamentals

Optical wave functions in free-space and quantum wave functions in field-free regions fulfil, respectively, the wave equation [1]

$$\nabla^2\Psi(\mathbf{r},\,t)=\frac{1}{c^2}\frac{\partial^2\Psi(\mathbf{r},\,t)}{\partial t^2},\tag{1}$$

with c the light speed in vacuum, and the Schrödinger equation [3]

$$-\frac{\hbar^2}{2m}\nabla^2\Psi(\mathbf{r},\,t)=i\hbar\frac{\partial\Psi(\mathbf{r},\,t)}{\partial t},\tag{2}$$

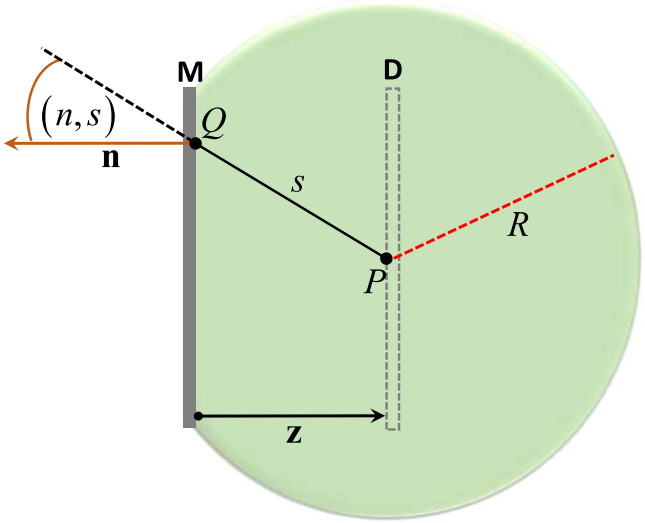

Figure 1. Conceptual sketch to describe optical and quantum interference with basis on the Helmholtz-Kirchhoff integral theorem.

with m the mass of the particle. In both cases, the time component of the wave function $\Psi(\mathbf{r},\,t)$ is harmonic and of the forms $\exp(\pm i\,\omega\,t)$ for equation (1), with ω the angular frequency of the wave, and $\exp(-iE\,t/\hbar)$ for equation (2), with E the particle energy; while the spatial component of $\Psi(\mathbf{r},\,t)$ is the solution of the Helmholtz equation

$$\nabla^2\psi(\mathbf{r})+k^2\,\psi(\mathbf{r})=0\tag{3}$$

under the specific boundary conditions due to the setup configuration. So, $\psi(\mathbf{r})=|\psi(\mathbf{r})|\exp[i\,\vartheta(\mathbf{r})]$ denotes the eigen-functions of the Laplacian operator with eigen-values $-k^2$, being $k=\omega/c$ in optics and $k=\sqrt{2mE}/\hbar$ in quantum mechanics.

The canonical form of the eigen-function is obtained from the Helmholtz-Kirchhoff integral theorem in equation (A2) (see appendix A). In order to use it for describing optical and quantum interference, let us consider the conceptual sketch in figure 1, i.e. the integration surface of the theorem is defined as a sphere, centered at P and with arbitrary long radius R, cut by the M plane, which is then included as a segment of such surface, thus being a part of the boundary condition. Furthermore, let us assume that the optical wave disturbance or single particle emerging from any point Q on the M plane is posteriorly detected at the point P on the D plane. s and z denote respectively the distances between the points Q and P, and between the planes M and D which configure the setup, as usual in optical as well as in quantum interference experiments.

Let us assume the well-known Kirchhoff's boundary conditions on the integration surface in figure 1 [11]. They stablish that the eigen-function ψ and its derivative nullify over the integration surface, except in the emitting region of waves or particles at the M plane, which includes the point Q, where $\psi(Q)=\psi_0\exp(iku)/u$, with ψ_0 a complex number, $-k^2$ the eigen-value of equation (3) and u the distance from

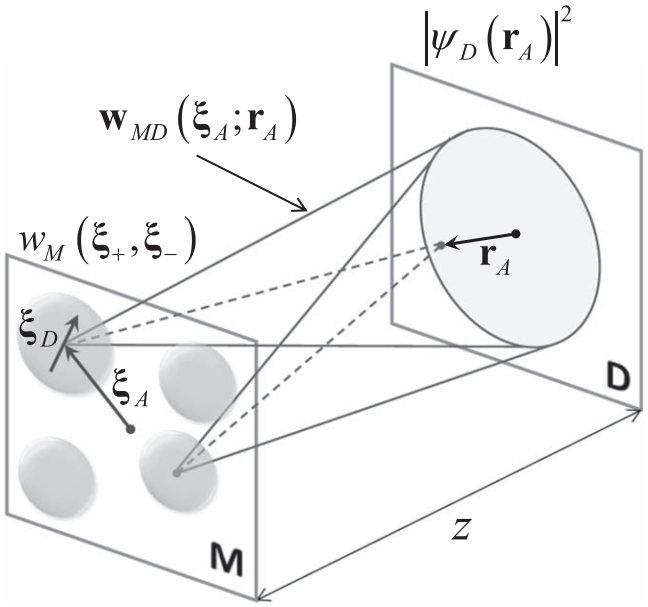

Figure 2. Conceptual sketch of the geometrical features of equations (7) and (8). Reduced coordinates are depicted by the arrows on the planes. The shadowed circles on the M plane represent structured supports of correlation. The shadowed circle on the D plane represents the detection area.

an external point source P_0 to the point Q on the integration surface. The segment $\overline{P_0Q} \equiv u$ makes an angle (n, u) with the normal to the integration surface at Q. It is reasonable that Kirchhoff's definition of $\psi(Q)$ has the same mathematical form of the Green's function of the system (appendix A), which is an eigen-function of equation (3). Indeed, it is an element of a base that allows expressing any boundary condition on the M plane. It is also apparent that $\psi(Q)$ should be necessarily defined from outside of the integration surface, in order to assure that it takes a part strictly as a boundary condition for the Helmholtz-Kirchhoff integral theorem in equation (A2). It has the practical consequence that this boundary condition can be experimentally controlled by means of the illumination of the M plane. In this sense, Kirchhoff's definition of $\psi(Q)$ allows to assign suitable amplitude and phase values to the boundary condition in order to represent a wide variety of emission events at the M plane, including optical waves, quantum particles, as well as deterministic and statistical processes. Furthermore, it is assumed that the condition

$$\lim_{R\to\infty} R\left(\frac{\partial\psi(R)}{\partial n} - ik\psi(R)\right) = 0,$$

due first to Sommerfeld [11], is achieved on the remaining spherical surface. So, the Kirchhoff's boundary conditions together with the Sommerfeld's condition assure that only the emitting region on the M plane contributes to the eigen-function $\psi(P)$ determined by the Helmholtz-Kirchhoff integral theorem. It is well-known that such boundary conditions are not mathematically rigorous; however, they lead to accurate results and therefore, they are widely assumed in interference modeling [11, 12].

The derivatives of the Green's function in the Helmholtz-Kirchhoff integral theorem in equation (A2) (appendix A) and of $\psi(Q)$ give respectively

$$\frac{\partial}{\partial n}\left(\frac{\exp(ik|\mathbf{r}|)}{|\mathbf{r}|}\right) = \frac{\partial}{\partial n}\left(\frac{\exp(iks)}{s}\right) = \left(ik - \frac{1}{s}\right)\frac{\exp(iks)}{s}\cos(n, s), \quad (4a)$$

and

$$\frac{\partial\psi}{\partial n} = \psi_0\frac{\partial}{\partial n}\left(\frac{\exp(iku)}{u}\right) = \psi_0\left(ik - \frac{1}{u}\right)\frac{\exp(iku)}{u}\cos(n, u). \quad (4b)$$

In order to make the boundary condition in equation (4*b*) independent from the position of the external point source, an arbitrary long distance u is assumed, so that equation (4*b*) reduces to

$$\frac{\partial\psi}{\partial n} = -ik\,\psi(Q), \quad (4c)$$

with $\psi(Q) = \psi_0\exp(iku)$ and $\cos(n, u) = -1$. Accordingly, equations (A2), (4*a*) and (4*c*) yield

$$\psi(P) = -i\frac{k}{4\pi}\int_M \psi(Q)(1 + \cos(n, s))\frac{\exp(iks)}{s}dS + \frac{1}{4\pi}\int_M \psi(Q)\cos(n, s)\frac{\exp(iks)}{s^2}dS, \quad (5)$$

where the integration is realized over the emitting region on the M plane. By denoting the points Q and P respectively with the position vectors $\boldsymbol{\xi}$ and $\mathbf{r}$, figure 1, it follows $s = |\mathbf{z} + \mathbf{r} - \boldsymbol{\xi}|$ and $\cos(n, s) = \frac{z}{s} = \frac{z}{|\mathbf{z}+\mathbf{r}-\xi c|}$. Elliminate c in the denominator Accordingly, equation (5) takes the form (in the following, the functions defined on a plane are suffixed with the plane label and the modes defined in a volume are suffixed by the labels of the planes that delimit the volume)

$$\psi_D(\mathbf{r}) = -i\frac{k}{4\pi}\int_M d^2\xi\ \psi_M(\boldsymbol{\xi})\left(\frac{z + |\mathbf{z} + \mathbf{r} - \boldsymbol{\xi}|}{|\mathbf{z} + \mathbf{r} - \boldsymbol{\xi}|^2}\right)\exp(ik|\mathbf{z} + \mathbf{r} - \boldsymbol{\xi}|) + \frac{1}{4\pi}\int_M d^2\xi\ \psi_M(\boldsymbol{\xi})\ \frac{z}{|\mathbf{z} + \mathbf{r} - \boldsymbol{\xi}|^3}\exp(ik|\mathbf{z} + \mathbf{r} - \boldsymbol{\xi}|). \quad (6)$$

This expression determines the eigen-function $\psi_D(\mathbf{r})$ in terms of a time-independent (static) modal expansion, whose kernel denotes 3D non-paraxial, scalar, geometric and deterministic modes, defined in the volume delimited by the M and D planes. The values of the eigen-function $\psi_M(\boldsymbol{\xi})$ at the emission region determine the expansion coefficients.

3. Non-locality and spatial modulation

For the development below, let us take into account the following considerations:

(i) The positions of pair of points at the M plane are denoted as $(\boldsymbol{\xi}_+, \boldsymbol{\xi}_-)$ and expressed in reduced coordinates $\boldsymbol{\xi}_\pm = \boldsymbol{\xi}_A \pm \boldsymbol{\xi}_D/2$, with $\boldsymbol{\xi}_A$ specifying the position of the midpoint in between and $\boldsymbol{\xi}_D$ denoting the separation vector of the pair, figure 2.
(ii) Single points on the D plane are denoted by $\mathbf{r}_A$, in order to have a uniform notation.
(iii) The fixed parameters $(\mathbf{z}, k)$ explicitly appear in the argument of the 3D non-paraxial modes, but they do not appear in the arguments of the other functions.

The physical observable in both optical and quantum interference is the energy delivered at the D plane by the arriving wave disturbances or particles, whose spatial distribution is described by $|\psi_D(\mathbf{r}_A)|^2$. This quantity is straightforwardly obtained by multiplying equation (6) by its complex conjugate, and can be expressed as

$$|\psi_D(\mathbf{r}_A)|^2 = \int_M d^2\xi_A \mathbf{w}_{MD}(\xi_A; \mathbf{r}_A), \tag{7}$$

with

$$\mathbf{w}_{MD}(\xi_A; \mathbf{r}_A) = \int_M d^2\xi_D w_M(\xi_+, \xi_-)\Phi_{MD}(\xi_+, \xi_-; \mathbf{r}_A; \mathbf{z}, k), \tag{8}$$

a 3D modal expansion in the volume delimited by the M and the D planes, whose coefficients are given by the two-point function $w_M(\xi_+, \xi_-) = |w_M(\xi_+, \xi_-)| \exp[i\,\Delta\vartheta_M(\xi_+, \xi_-)] = \psi_M(\xi_+)\psi_M^*(\xi_-)$, with $\Delta\vartheta_M(\xi_+, \xi_-) = \vartheta_M(\xi_+) - \vartheta_M(\xi_-)$, defined over the emitting region on the M plane, and whose kernel denotes the 3D geometric, scalar, deterministic and non-paraxial modes

$$\begin{aligned}\Phi_{MD}(\boldsymbol{\xi}_+, \boldsymbol{\xi}_-; \mathbf{r}_A; \mathbf{z}, k) &= \frac{1}{(4\pi)^2}\left[k^2\left(\frac{z + |\mathbf{z} + \mathbf{r}_A - \boldsymbol{\xi}_+|}{|\mathbf{z} + \mathbf{r}_A - \boldsymbol{\xi}_+|^2}\right)\right.\\ &\times\left(\frac{z + |\mathbf{z} + \mathbf{r}_A - \boldsymbol{\xi}_-|}{|\mathbf{z} + \mathbf{r}_A - \boldsymbol{\xi}_-|^2}\right) + ik\left(\frac{z}{|\mathbf{z} + \mathbf{r}_A - \boldsymbol{\xi}_+|^3}\right)\\ &\times\left(\frac{z + |\mathbf{z} + \mathbf{r}_A - \boldsymbol{\xi}_-|}{|\mathbf{z} + \mathbf{r}_A - \boldsymbol{\xi}_-|^2}\right) - ik\left(\frac{z + |\mathbf{z} + \mathbf{r}_A - \boldsymbol{\xi}_+|}{|\mathbf{z} + \mathbf{r}_A - \boldsymbol{\xi}_+|^2}\right)\\ &\times\left(\frac{z}{|\mathbf{z} + \mathbf{r}_A - \boldsymbol{\xi}_-|^3}\right) + \left(\frac{z}{|\mathbf{z} + \mathbf{r}_A - \boldsymbol{\xi}_+|^3}\right)\\ &\times\left.\left(\frac{z}{|\mathbf{z} + \mathbf{r}_A - \boldsymbol{\xi}_-|^3}\right)\right]\\ &\times \exp(ik\,|\mathbf{z} + \mathbf{r}_A - \boldsymbol{\xi}_+| - ik\,|\mathbf{z} + \mathbf{r}_A - \boldsymbol{\xi}_-|),\end{aligned} \tag{9}$$

defined in the volume delimited by the M and D planes, too. So, equation (9) points out that there is a mode connecting a given pair of points on the M plane, with midpoint ξ_A and separation ξ_D, with a specific point $\mathbf{r}_A$ on the D plane. In turn, the 3D modal expansion in equation (8) relates a specific point ξ_A on the M plane with a given point $\mathbf{r}_A$ on the D plane, by adding the contributions of all the pairs with midpoint ξ_A for which the non-local function $w_M(\xi_+, \xi_-)$ takes on non-null values. The region determined by the set of such pairs of points is called the structured support of correlation [13, 14] centered at ξ_A. Finally, equation (7) indicates that $|\psi_D(\mathbf{r}_A)|^2$ results from the addition of the 3D modal expansions for all points ξ_A in the emitting region on the M plane.

It is worth noting that

(i) the non-paraxial modes and the non-local function have Hermitic symmetry, i.e. $\Phi_{MD}(\xi_+, \xi_-; \mathbf{r}_A; \mathbf{z}, k) = \Phi_{MD}^*(\xi_-, \xi_+; \mathbf{r}_A; \mathbf{z}, k)$ and $w_M(\xi_+, \xi_-) = w_M^*(\xi_-, \xi_+)$, with the asterisk denoting complex conjugate, and
(ii) the non-local function $w_M(\xi_+, \xi_-)$ includes the local component $w_M(\xi_A, \xi_A) = |\psi_M(\xi_A)|^2$, i.e. its values at the individual points ξ_A for $\xi_D = 0$.

Consequently, the local component of the non-local function $w_M(\xi_+, \xi_-)$ is connected with the point $\mathbf{r}_A$ by the real valued and positive definite kernel modes

$$\Phi_{MD}(\xi_A; \mathbf{r}_A; \mathbf{z}, k) = \frac{1}{(4\pi)^2}\left[k^2\left(\frac{z + |\mathbf{z} + \mathbf{r}_A - \xi_A|}{|\mathbf{z} + \mathbf{r}_A - \xi_A|^2}\right)^2 + \left(\frac{z}{|\mathbf{z} + \mathbf{r}_A - \xi_A|^3}\right)^2\right], \tag{10}$$

so that, the modal expansion that this local component contributes is given by

$$\mathbf{w}_{MD}^{(R)}(\xi_A; \mathbf{r}_A) = |\psi_M(\xi_A)|^2\Phi_{MD}(\xi_A; \mathbf{r}_A; \mathbf{z}, k). \tag{11}$$

In turn, the 3D modal expansion $\mathbf{w}_{MD}^{(V)}(\xi_A; \mathbf{r}_A)$, given by equation (8) for $\xi_D \neq 0$, adds the integrand values for the two degrees of freedom in orientation of the separation vector ξ_D of each contributing pair of points on the M plane. So, by taking into account the Hermitic symmetry of the integrand, this modal expansion becomes

$$\begin{aligned}\mathbf{w}_{MD}^{(V)}(\xi_A; \mathbf{r}_A) = 2\int_{\substack{M\\ \xi_D\neq 0}} d^2\xi_D\ &|w_M(\xi_+, \xi_-)|\\ &\times \mathrm{Re}\,[\Phi_{MD}(\xi_+, \xi_-; \mathbf{r}_A; \mathbf{z}, k)\\ &\times \exp(i\Delta\vartheta_M(\xi_+, \xi_-))],\end{aligned} \tag{12}$$

with Re denoting the real part, and

$$
\begin{aligned}
&2\,\mathrm{Re}\left[\Phi_{MD}(\xi_+,\,\xi_-;\,\mathbf{r}_A;\,\mathbf{z},\,k)\,\exp\left(i\Delta\vartheta_M(\xi_+,\,\xi_-)\right)\right]\\
&=\frac{2}{(4\pi)^2}\Bigg[k^2\left(\frac{z+|\mathbf{z}+\mathbf{r}_A-\xi_+|}{|\mathbf{z}+\mathbf{r}_A-\xi_+|^2}\right)\left(\frac{z+|\mathbf{z}+\mathbf{r}_A-\xi_-|}{|\mathbf{z}+\mathbf{r}_A-\xi_-|^2}\right)\\
&\quad+\left(\frac{z}{|\mathbf{z}+\mathbf{r}_A-\xi_+|^3}\right)\left(\frac{z}{|\mathbf{z}+\mathbf{r}_A-\xi_-|^3}\right)\Bigg]\\
&\quad\times\cos\left(k|\mathbf{z}+\mathbf{r}_A-\xi_+|-k|\mathbf{z}+\mathbf{r}_A-\xi_-|+\Delta\vartheta_M(\xi_+,\,\xi_-)\right)\\
&\quad-\frac{2k}{(4\pi)^2}\Bigg[\left(\frac{z}{|\mathbf{z}+\mathbf{r}_A-\xi_+|^3}\right)\left(\frac{z+|\mathbf{z}+\mathbf{r}_A-\xi_-|}{|\mathbf{z}+\mathbf{r}_A-\xi_-|^2}\right)\\
&\quad-\left(\frac{z+|\mathbf{z}+\mathbf{r}_A-\xi_+|}{|\mathbf{z}+\mathbf{r}_A-\xi_+|^2}\right)\left(\frac{z}{|\mathbf{z}+\mathbf{r}_A-\xi_-|^3}\right)\Bigg]\\
&\quad\times\sin\left(k\,|\mathbf{z}+\mathbf{r}_A-\xi_+|-k\,|\mathbf{z}+\mathbf{r}_A-\xi_-|+\Delta\vartheta_M(\xi_+,\,\xi_-)\right)
\end{aligned}
\tag{13}
$$

is the 3D non-paraxial kernel defined in the volume between the M and D planes. It is apparent that $\mathbf{w}^{(V)}_{MD}(\xi_A;\,\mathbf{r}_A)$ is real valued too, but take on positive and negative values due to the harmonic oscillations of the kernel. Furthermore, equations (11) and (12) point out that the 3D non-paraxial modal expansion in equation (8) can be expressed as

$$
\mathbf{w}_{MD}(\xi_A;\,\mathbf{r}_A)=\mathbf{w}^{(R)}_{MD}(\xi_A;\,\mathbf{r}_A)+\mathbf{w}^{(V)}_{MD}(\xi_A;\,\mathbf{r}_A),
\tag{14}
$$

that reduces to $\mathbf{w}_{MD}(\xi_A;\,\mathbf{r}_A)=\mathbf{w}^{(R)}_{MD}(\xi_A;\,\mathbf{r}_A)$ for the pairs of points at which the non-local function $w_M(\xi_+,\,\xi_-)$ nullifies.

In order to interpret the 3D non-paraxial modal expansions in equation (14) geometrically, let us consider a given point ξ_A on the M plane and all the points $\mathbf{r}_A$ on the detection area of the D plane. Thus, each modal expansion determines a cone in the volume between the M and D planes, with vertex on ξ_A and basis on the detection area, as conceptually depicted in figure 2. It can be exemplified at the scales of interest by considering a pair of points on the emission region, at the positions $\xi_A=\pm\mathbf{b}/2$, so that $\xi_D=\mathbf{b}$, with $\mathbf{b}$ and z comparable with the wavelength, for instance $|\mathbf{b}|=3\lambda$ and $0\leqslant z\leqslant 5\lambda$, with $\lambda=4$ pm for quantum particles and $\lambda=0.632\ \mu$m for optical waves. Figure 3 illustrates important geometric features of the cones corresponding to the 3D modal expansions:

(i) The geometry of the cones is the same for optical waves and quantum particles, but their scales clearly differ, due to the parameter $k=2\pi/\lambda$. The cones $\mathbf{w}^{(R)}_{MD}(\xi_A;\,\mathbf{r}_A)$ have the same Lorentzian cross-section and angular aperture no matter the position of their vertices at the M plane, as shown in (a) and (e). The fringe modulation of the cones $\mathbf{w}^{(V)}_{MD}(\xi_A;\,\mathbf{r}_A)$ exhibits spatial frequency chirping due to the non-linear argument of the harmonic function of the modes in equation (13), and Lorentzian envelope due to the coefficients of such harmonic function, as shown in (b), (f).

(ii) The cones $\mathbf{w}^{(R)}_{MD}(\xi_A;\,\mathbf{r}_A)$ are unable to produce interference spatial modulation as they overlap, as shown by $\mathbf{w}^{(R)}_{MD}(\mathbf{b}/2;\,\mathbf{r}_A)+\mathbf{w}^{(R)}_{MD}(-\mathbf{b}/2;\,\mathbf{r}_A)$ in (a) and (e).

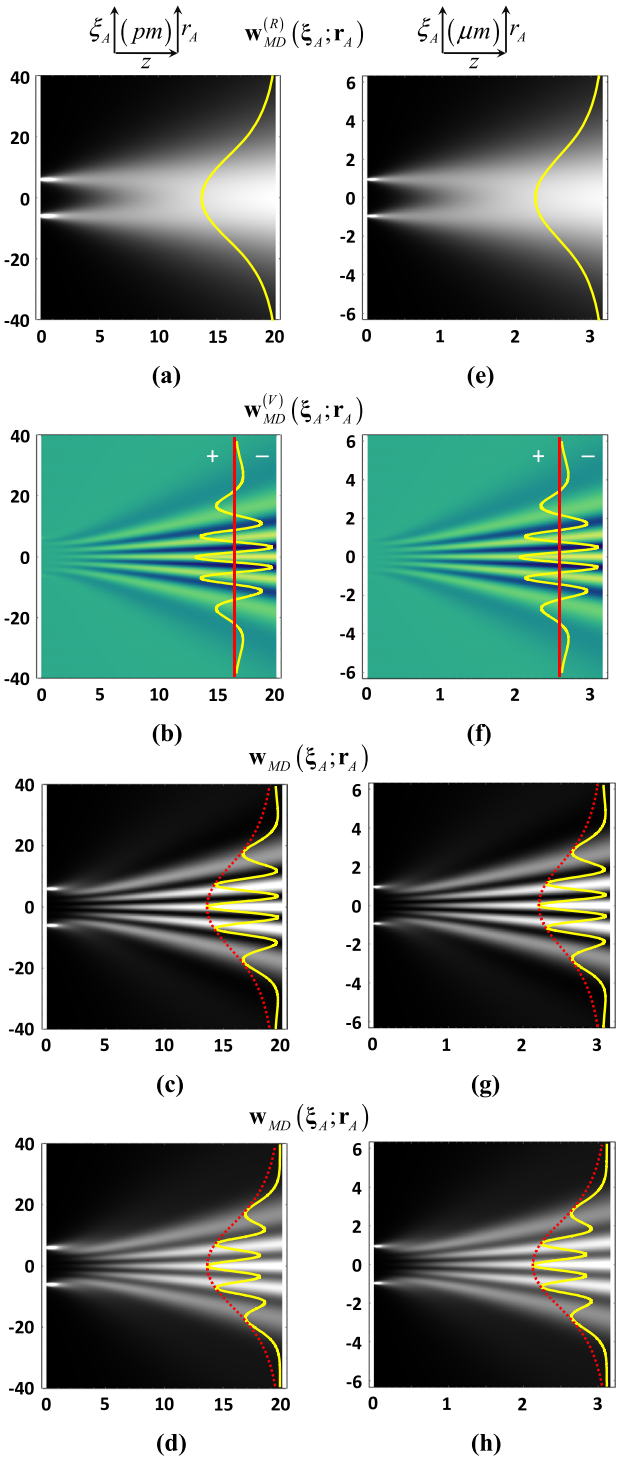

Figure 3. Illustrating the geometrical features of equations (11), (12) and (14) for a pair of points with separation $|\mathbf{b}|=3\lambda$, and $\lambda=4$ pm for the column of the left and $\lambda=0.632\ \mu$m for the column on the right. Graphs on the top row are obtained for $w_M(\mathbf{b})=0$. Graphs on the third and fourth rows are obtained by adding the corresponding graphs on the top and the second row for the maximal value of $w_M(\mathbf{b})$ (highest correlated pair of points) in (c), (g), and for a half of this value (partially correlated pair of points) in (d), (h). The graphs are enhanced for presentation purposes and the vertical profiles describe the cross-section of the respective cones at $z=5\lambda$, with their Lorentzian envelopes in dotted lines.

(iii) Interference spatial modulation results only by overlapping $\mathbf{w}_{MD}^{(V)}(\xi_A;\,\mathbf{r}_A)$ on $\mathbf{w}_{MD}^{(R)}(\xi_A;\,\mathbf{r}_A)$, as expressed in equation (14). Indeed, the overlap of $\mathbf{w}_{MD}^{(V)}(0;\,\mathbf{r}_A)$ in (b) and (f) on the corresponding $\mathbf{w}_{MD}^{(R)}(\mathbf{b}/2;\,\mathbf{r}_A) + \mathbf{w}_{MD}^{(R)}(-\mathbf{b}/2;\,\mathbf{r}_A)$ in (a) and (e) gives the interference modulated cone $\mathbf{w}_{MD}(\xi_A;\,\mathbf{r}_A)$ in (c), (d), (g) and (h).

(iv) The non-local function $w_M(\xi_+,\,\xi_-)$ at the M plane weights the spatial modulation contributed by $\mathbf{w}_{MD}^{(V)}(\xi_A;\,\mathbf{r}_A)$. In order to explain it clearly, let us assume that the eigenfunction $\psi_M(\xi_\pm)$ is normalized. As a consequence, $0 \leqslant |w_M(\xi_+,\,\xi_-)| \leqslant 1$. So, the strongest modulation (high contrasted interference), obtained by $|w_M(\xi_+,\,\xi_-)| = 1$, is smoothed (low contrasted interference) by $|w_M(\xi_+,\,\xi_-)| < 1$ and disappears completely by $|w_M(\xi_+,\,\xi_-)| = 0$, as illustrated in (c) and (g) for $w_M(\mathbf{b}) = 1$, in (d) and (h) for $w_M(\mathbf{b}) = 0.5$ and in (a) and (e) for $w_M(\mathbf{b}) = 0$.

(v) The phase $\Delta\vartheta_M(\xi_+,\,\xi_-)$ of the non-local function only shifts laterally the fringe modulation of the modes in equation (13).

The emission of optical waves and quantum particles are, in general, statistical processes. It confers statistical features to optical and quantum interference [1, 15], whose individual realizations are characterized by equations (7) and (14). An individual realization begins with the emission event of a wave disturbance or a single particle at the external source, followed by its crossing of the M plane and ends with its detection at the D plane. Furthermore, in quantum interference there is only a single particle moving in the setup in any individual realization, and its behavior is not affected by the particles in preceding individual realizations and cannot affect the behavior of the particles in posterior individual realizations.

The experimental outcomes result by averaging the statistical ensemble of a great enough number of individual realizations occurred during the detection. This ensemble average, represented by the symbol $\langle\ \rangle$, involves only the non-local function $w_M(\xi_+,\,\xi_-)$ in equations (11) and (12), because the 3D non-paraxial modes in equations (10) and (13) are deterministic functions.

Thus, the ensemble average gives the two-point correlation $W_M(\xi_+,\,\xi_-) = \langle w_M(\xi_+,\,\xi_-)\rangle$ at the M plane which leads to the physical observable outcome $S_D(\mathbf{r}_A) = \langle|\psi_D(\mathbf{r}_A)|^2\rangle$ at the D plane. It is related to the spatial distribution at the D plane of the power spectrum of the optical interference pattern [1, 13], as well as of the expected detections of particles in quantum interference [3, 15], respectively. In other words, equations (10) and (13) characterize the 3D non-paraxial kernel for the two-point correlation modelling in optical and quantum interference at the micro and nano-scales.

This analysis leads to the conclusion that non-locality is a necessary condition for both optical and quantum interference. Specifically, the geometry of the spatial modulation is completely determined by the modes in equation (13), while the modulation strength is determined by the values of the associated $w_M(\xi_+,\,\xi_-)$ for $\xi_D \neq 0$, in each individual realization of the two-point correlation $W_M(\xi_+,\,\xi_-)$. It means that the emitted optical waves and quantum particles fill the cones in equation (14) after a great enough number of individual realizations, as illustrated in figure 3.

The requirement of non-locality in optical and quantum interference underlines the relevance of the non-local function $w_M(\xi_+,\,\xi_-)$ and the two-point correlation $W_M(\xi_+,\,\xi_-)$ in the theoretical description and modelling of such phenomena. This description was performed in optics by the well-known theory of optical coherence [1], but a useful non-paraxial modeling for the micro and nano-scales has been not yet reported. To our knowledge, a similar situation occurs in single particle quantum interference, although the quantum theory of optical coherence is well-stablished since a long time [16].

Consequently, the preparation of the non-local function $w_M(\xi_+,\,\xi_-)$ at the boundary condition specified on the M plane (in usual experiments it is a mask with openings) is the key to obtain interference patterns at the D plane (see appendix B for details). Such patterns are determined by the cross-sections at such plane of the overlapped modulated cones $\mathbf{w}_{MD}(\xi_A;\,\mathbf{r}_A)$, described by equation (8), which are filled by the optical waves and the quantum particles after a great enough number of individual realizations. It is expressed as

$$S_D(\mathbf{r}_A) = S_D^{(R)}(\mathbf{r}_A) + S_D^{(V)}(\mathbf{r}_A), \tag{15}$$

whose terms are obtained, respectively, by replacing equation (14) in equation (8) and then by applying the ensemble average. So, $S_D^{(R)}(\mathbf{r}_A) \geqslant 0$ is determined by the cross-section of the overlapped cones $\mathbf{w}_{MD}^{(R)}(\xi_A;\,\mathbf{r}_A)$, as illustrated by the vertical profiles in figures 3(a), (e), while $S_D^{(V)}(\mathbf{r}_A)$ is determined by the cross-section of the overlapped cones $\mathbf{w}_{MD}^{(V)}(\boldsymbol{\xi}_A;\,\mathbf{r}_A)$, which takes on positive and negative values, as illustrated by the vertical profiles in figures 3(b), (f). It implies a restriction on the 3D non-paraxial kernel due to the condition $S_D^{(R)}(\mathbf{r}_A) \geqslant |S_D^{(V)}(\mathbf{r}_A)|$ for $S_D^{(V)}(\mathbf{r}_A) < 0$, because equation (15) is positive definite. Indeed, equations (8) and (15) yield

$$\int_D d^2r_A\,|\psi_D(\mathbf{r}_A)|^2 = \int_M d^2\xi_A \int_D d^2r_A\ \mathbf{w}_{MD}^{(R)}(\xi_A;\,\mathbf{r}_A) + \int_M d^2\xi_A \int_D d^2r_A\,\mathbf{w}_{MD}^{(V)}(\xi_A;\,\mathbf{r}_A),$$

with

$$\int_M d^2\xi_A \int_D d^2r_A\,\mathbf{w}_{MD}^{(R)}(\xi_A;\,\mathbf{r}_A) = \int_M d^2\xi_A\ |\psi_M(\boldsymbol{\xi}_A)|^2 \int_D d^2r_A\,\Phi_{MD}(\boldsymbol{\xi}_A;\,\mathbf{r}_A;\,\mathbf{z},\,k),$$

according to equation (11), and

$$\int_M d^2\xi_A \int_D d^2r_A\,\mathbf{w}_{MD}^{(V)}(\xi_A;\,\mathbf{r}_A) = \int_M d^2\xi_A \int_{\substack{M\\ \boldsymbol{\xi}_D\neq 0}} d^2\xi_D\ w_M(\xi_+,\,\xi_-) \times \int_D d^2r_A\ \Phi_{MD}(\xi_+,\,\xi_-;\,\mathbf{r}_A;\,\mathbf{z},\,k)$$

according to equation (12). These expressions together with the energy conservation law

$$\int_D d^2r_A\ |\psi_D(\mathbf{r}_A)|^2 = \int_D d^2\xi_A\ |\psi_M(\boldsymbol{\xi}_A)|^2$$

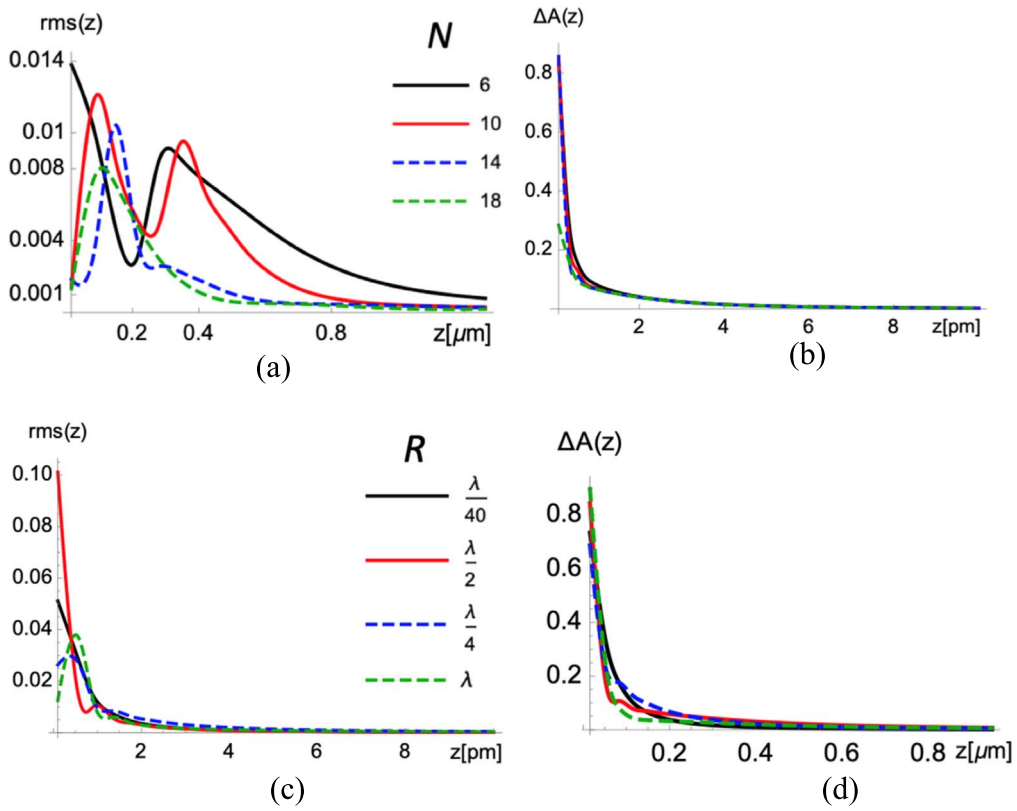

Figure 4. Descriptors in equations (19) and (20) for a ring of radius $R = \lambda/2$ and N vertices of $\mathbf{w}_{MD}^{(R)}(\xi_A; \mathbf{r}_A)$-cones uniformly distributed on the M plane in (a) and (b). A ring of increasing radius $(\lambda/40) \leqslant R \leqslant \lambda$ and $N = 9$ uniformly distributed vertices is considered in (c) and (d). Full spatial correlation is assumed in all the graphs and $(\lambda/40) \leqslant z \leqslant 2\lambda$. The comparison performed in (a) and (d) is for optical waves of $\lambda = 0.632$ μm, and in (b) and (c) is for particles of de Broglie wavelength $\lambda = 4$ pm.

for each individual realization, yield

$$\int_D d^2 r_A \;\; \Phi_{MD}(\xi_A; \mathbf{r}_A; \mathbf{z}, k) = 1, \tag{16a}$$

and

$$\int_D d^2 r_A \;\; \Phi_{MD}(\xi_+, \xi_-; \mathbf{r}_A; \mathbf{z}, k) = 0 \tag{16b}$$

for the cross-section of the 3D non-paraxial mode associated to any pair of points (ξ_+, ξ_-), at any distance z from the M plane. The vertical profiles illustrated in figures 3(a), (e) and (b), (f) are in accordance with conditions in equations (16*a*) and (16*b*) respectively. In spite that images in figure 3 illustrate a particular case of equations (11), (12) and (14), they are of general interest, because the geometrical features of the contributions of any spatially correlated pair of points to both optical and quantum interference have similar shape (i.e. Lorentzian envelopes and fringe modulation whose spatial distribution depends on the pair separation). So, in accordance with the modal expansion in equation (8), the spatial modulation of interference with any set of correlated points can be obtained by overlapping the contributions of all the pairs of points in the set, whose geometric features are similar to those illustrated in figure 3.

It is worth remarking that the 3D non-paraxial kernel of the two-point correlation is the same for both optical and quantum interference, thus offering a unified framework to describe the spatial features of these physical phenomena. Because the kernel is essentially determined by the boundary conditions imposed by the setup, it gives a central role to the experimental arrangement, i.e. the spatial modulation established by the kernel in the setup volume emerges as the necessary cause of interference. Specifically, the spatial modulation in the volume delimited by the M and D planes is mainly due to the configuration of the mask placed at the M plane and is activated by the non-local function prepared at this plane. As explained in appendix B, the preparation of the non-local function occurs in the volume delimited by a previous S plane and the M plane, and closely depends on the configuration of the effective source of waves or particles placed at the S plane. It suggests that the setup configuration is crucial to determinate the non-locality required by interference, a feature conventionally attributed only to the optical field and to the quantum wave function. In addition, the model accounts for each individual experimental realization and describes the interference pattern formation as the accumulation of the detection events of such individual realizations. These features provide a new physical insight for both optical and quantum interference.

4. Accuracy discussion

Let us estimate the contributions of the terms of equations (10) and (13) to the 3D non-paraxial kernel along the propagation z-axis. It is relevant because the difference in the decay rate of such terms along this axis should provide a criterion to determine the size of the region in which their contributions cannot be neglected. For instance, the terms of

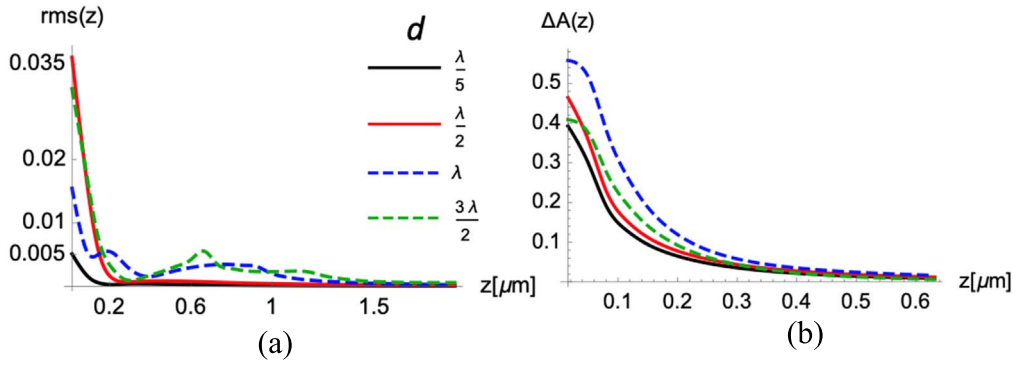

Figure 5. Descriptors of equations (19) and (20) for three parallel slits at the M plane, each one enclosing a uniform linear array of 10 vertices of $\mathbf{w}_{MD}^{(R)}(\xi_A;\, \mathbf{r}_A)$-cones with spacing $\lambda/10$, for optical interference with waves of $\lambda = 0.632\ \mu$m. The curves were calculated for different slit spacing d under maximal spatial correlation.

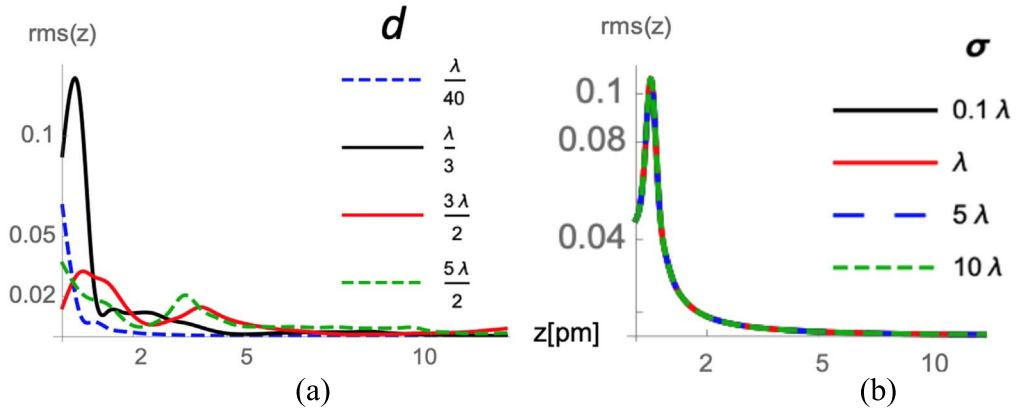

Figure 6. Descriptors in equations (19) and (20) for a thin slit at the M plane enclosing a uniformly distributed linear array of vertices of $\mathbf{w}_{MD}^{(R)}(\xi_A;\, \mathbf{r}_A)$-cones for quantum interference with particles of de Broglie wavelength $\lambda = 4$ pm. In (a) the array contains 10 vertices with different spacing d under maximal correlation. In (b) the array of length λ contains 8 vertices under Gaussian correlation controled by the standard deviation σ. The horizontal axis in both graphs is z [pm].

equation (10) decay like z^{-2} and z^{-4} respectively, while in equation (13) the cosine terms decay like z^{-2} and z^{-4} respectively, and the sine terms decay like z^{-3}. It is apparent that the first terms of equations (10) and (13) have the same decay along the z-axis, with the slowest decay rate. Therefore, these terms should characterize the kernel. However, this paper is focused on short propagation distances, in which all the terms should be taken into account to provide an accurate prediction.

A comparative analysis is performed by means of two descriptors, which compare the power spectrum $S_D(\mathbf{r}_A)$, obtained with the whole kernel in equations (10) and (13), with the power spectrum $S'_D(\mathbf{r}_A)$ obtained with the reduced kernel of terms

$$\Phi'_{MD}(\xi_A;\, \mathbf{r}_A;\, \mathbf{z},\, k) = \left(\frac{k}{4\pi}\right)^2 \left(\frac{z + |\mathbf{z} + \mathbf{r}_A - \xi_A|}{|\mathbf{z} + \mathbf{r}_A - \xi_A|^2}\right)^2, \quad (17)$$

and

$$2\,\mathrm{Re}\,[\Phi'_{MD}(\xi_+,\, \xi_-;\, \mathbf{r}_A;\, \mathbf{z},\, k)\ \exp\,(i\Delta\vartheta_M(\xi_+,\, \xi_-))]$$
$$= 2\left(\frac{k}{4\pi}\right)^2 \left(\frac{z + |\mathbf{z} + \mathbf{r}_A - \xi_+|}{|\mathbf{z} + \mathbf{r}_A - \xi_+|^2}\right) \left(\frac{z + |\mathbf{z} + \mathbf{r}_A - \xi_-|}{|\mathbf{z} + \mathbf{r}_A - \xi_-|^2}\right)$$
$$\times \cos\,(k\,|\mathbf{z} + \mathbf{r}_A - \xi_+| - k\,|\mathbf{z} + \mathbf{r}_A - \xi_-| + \Delta\vartheta_M(\xi_+,\, \xi_-)). \quad (18)$$

The descriptors are

$$rms(z) = \sqrt{\frac{1}{D}\int_D d^2 r_A [\tilde{S}_D(\mathbf{r}_A) - \tilde{S}'_D(\mathbf{r}_A)]^2}\,, \quad (19)$$

where D is the integration area on the D plane, and $\tilde{S}_D(\mathbf{r}_A)$ and $\tilde{S}'_D(\mathbf{r}_A)$ are the normalized versions of $S_D(\mathbf{r}_A)$ and $S'_D(\mathbf{r}_A)$ respectively, i.e. $\frac{1}{D}\int_D d^2 r_A\ \tilde{S}_D(\mathbf{r}_A) = \frac{1}{D}\int_D d^2 r_A\ \tilde{S}'_D(\mathbf{r}_A) = 1$. So, the descriptor $0 < rms(z) < 1$ compares the morphology of $S_D(\mathbf{r}_A)$ and $S'_D(\mathbf{r}_A)$ on the D plane for $z > 0$, i.e. along the propagation axis; and

$$\Delta A(z) = |1 - (A_{S'}(z)/A_S(z))| \quad (20)$$

with $A_{S'}(z) = \frac{1}{D}\int_D d^2 r_A S'_D(\mathbf{r}_A)$ and $A_S(z) = \frac{1}{D}\int_D d^2 r_A S_D(\mathbf{r}_A)$, and the integrals are performed on the same area at the D plane for $z > 0$. Thus, the descriptor $0 < \Delta A(z) < 1$ compares the area under the curves $S_D(\mathbf{r}_A)$ and $S'_D(\mathbf{r}_A)$ along the propagation axis. Therefore, $rms(z) \to 0$ and $\Delta A(z) \to 0$ mean $S_D(\mathbf{r}_A) \cong S'_D(\mathbf{r}_A)$ so that the reduced kernel, whose terms are given by equations (17) and (18), is accurate enough for 3D non-paraxial description of the wave and particle propagation. This accuracy is assured in more than 99% for $rms(z) \leqslant 0.01$ and $\Delta A(z) \leqslant 0.01$.

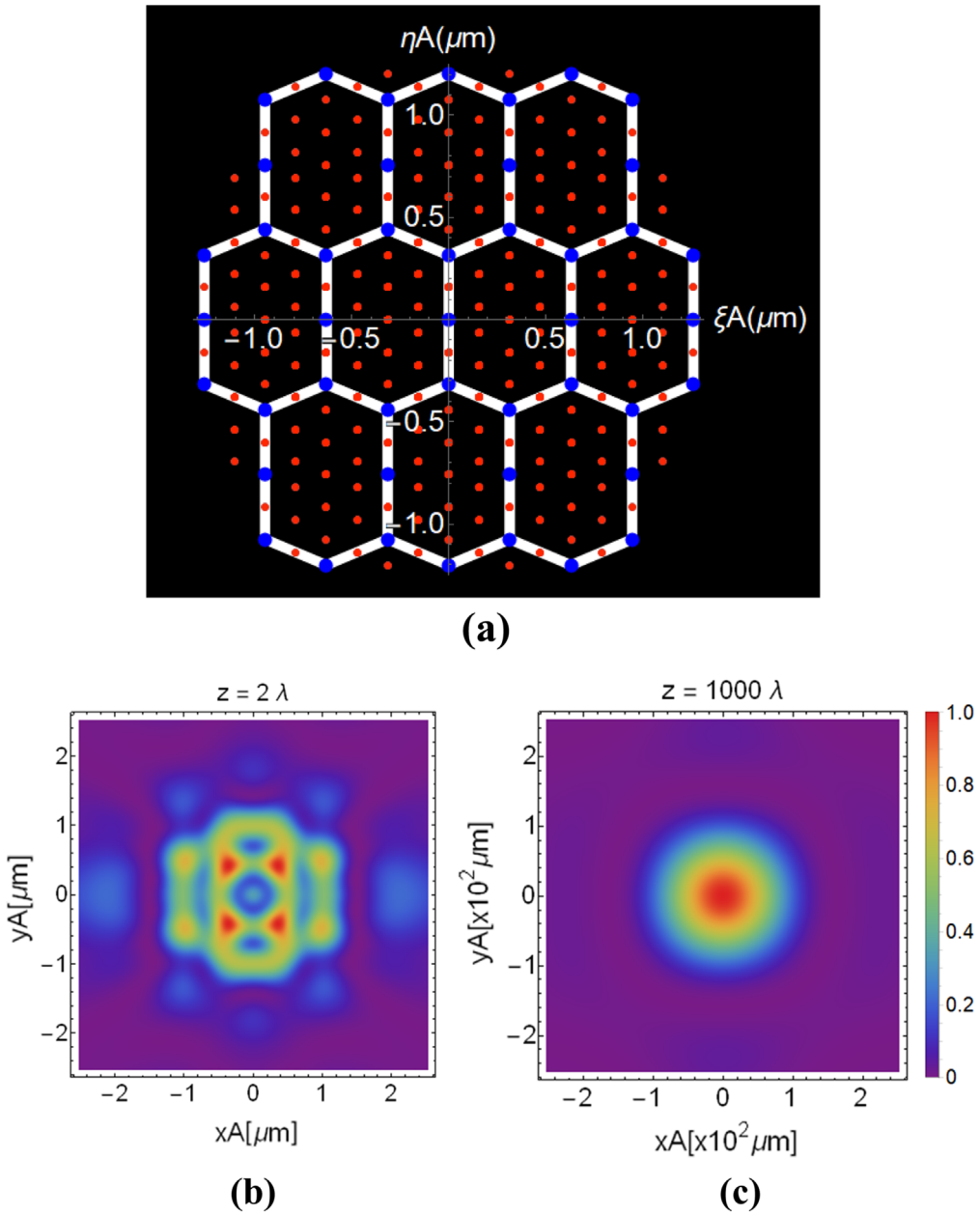

Figure 7. Honeycomb grating for optical interference ($\lambda = 0.632\ \mu$m) under full spatial correlation. (a) Mask with 10 identical hexagonal frame openings in thick solid white line on an area of $4\lambda \times 4\lambda$. Blue dots represent the vertices of $\mathbf{w}_{MD}^{(R)}(\xi_A;\ \mathbf{r}_A)$-cones and red dots are the vertices of $\mathbf{w}_{MD}^{(V)}(\xi_A;\ \mathbf{r}_A)$-cones. Pseudo-color is used for the power spectrum of the interference patterns, described by equation (15), are shown for $z = 2\lambda$ in (b) and $z = 1000\lambda$ in (c).

Figures 4–6 show that both descriptors tend asymptotically to null as z increases, independently from specific features (i.e. number and density of cone vertices distributed on the M plane, geometry of the vertices distribution, spatial correlation prepared at the M plane, wavelength). This behavior allows to estimate the limit propagation distance z_0 such that the conditions $rms(z) \leqslant 0.01$ and $\Delta A(z) \leqslant 0.01$ are fulfilled for $z \geqslant z_0$ for any considered feature. It means that the reduced kernel can be regarded as exact for $z \geqslant z_0$, while the complete kernel should be taken into account for $z < z_0$. The limit distance $z_0 = \lambda/2$ achieves these requirements, as illustrated in figures 4–6. As a consequence, the reduced kernel can be regarded as exact for describing the propagation of both optical waves and quantum particles at the micro and nano-scales.

Furthermore, the descriptors point out that the differences between $S_D(\mathbf{r}_A)$ and $S_D'(\mathbf{r}_A)$ for $z < \lambda/2$ are mainly in area under the curves, while the morphology differences are not significant. It means that the reduced kernel gives also a well-approached description for $z < \lambda/2$.

The vertices of $\mathbf{w}_{MD}^{(R)}(\xi_A;\ \mathbf{r}_A)$-cones are uniformly distributed on a ring under full spatial correlation in figure 4. The radius of the ring is fixed in (a) and (b) and the number of vertices grows, thus increasing the vertex density. The kernel morphologies are compared for optical interference in (a), while

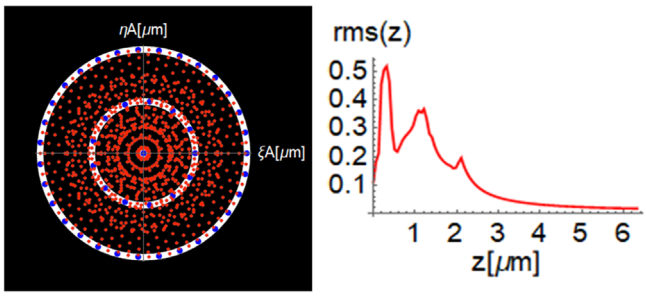

Figure 8. (a) Nano-structured mask composed by a central hole and two thin concentric rings with outer diameter 4λ ($\lambda = 0.632\mu m$). 45 vertices of $\mathbf{w}_{MD}^{(R)}(\xi_A; \mathbf{r}_A)$-cones are uniformly distributed, 31 on the outer ring, 13 on the inner ring and 1 in the hole. The red dots represent the vertices of $\mathbf{w}_{MD}^{(V)}(\xi_A; \mathbf{r}_A)$-cones. The mask is uniformly illuminated under maximal spatial correlation. The *rms*-descriptor in (b) compares the diffraction patterns produced by the masks in (a) and in figure 7(a), described by equation (15), along the propagation z-axis.

the areas under the curves are compared for quantum interference in (b). Similar graphs of the *rms* and the $\Delta A(z)$-descriptors are obtained for quantum and optical interferece respectively, with the appropriate scales on the z-axis. In (c) and (d), the number of vertices of $\mathbf{w}_{MD}^{(R)}(\xi_A; \mathbf{r}_A)$-cones is fixed and the ring radius increases. Now, the kernel morphologies are compared for quantum interference in (c), while the areas under the curves are compared for optical interference in (d). Once more, similar graphs of the *rms* and the $\Delta A(z)$-descriptors are obtained for optical and quantum interference respectively, with the appropriate scales on the z-axis. All the graphs in figure 4 confirm the $\lambda/2$-criterion.

The kernel morphologies and their areas under the curves are compared in figure 5 for optical interference produced by three thin parallel slits with different spacing. Each slit encloses a uniform linear array of vertices of $\mathbf{w}_{MD}^{(R)}(\xi_A; \mathbf{r}_A)$-cones, under full spatial correlation. The graphs confirm the $\lambda/2$-criterion in all cases, and the same result is obtained for quantum interference with the only difference in the scale of the z-axis, in accordance to the de Broglie wavelenght.

The descriptors in figure 6 compare the kernel morphologies (a) and the areas under the curves (b) for quantum interference produced by single particles that cross a thin slit, enclosing a uniform linear array of vertices of $\mathbf{w}_{MD}^{(R)}(\xi_A; \mathbf{r}_A)$-cones. The number of vertices is fixed in all graphs, and different vertex spacing and full spatial correlation is considered in (a), while the vertex spacing is fixed and variable Gaussian spatial correlation is assumed in (b). Once more, the $\lambda/2$-criterion is confirmed in all situations. The same result is obtained for optical interference with the only diference in the in the scale of the propagation z-axis, in accordance with the optical wavelenght.

Although particular experimental situations have been considered in figures 4–6, they confirm the $\lambda/2$-criterion independently from specific features involved in both optical and quantum interference. So, the general validity of this criterion is expectable, and allows us to use the reduced kernel for the exact modeling of both optical and quantum interference at the micro and nano-scales.

It is interesting to note that the spatial correlation kernel and the kernel for modeling the non-paraxial propagation of the optical and the quantum wave functions are related, as shown by equations (6)–insert (9). Both kernels predict exactly the same physical observable, determined by the square modulus of the wave function, in fully spatially correlated interference. So, they have the same accuracy in such cases. Nevertheless, the wave function kernel cannot account for partially correlated interference, and therefore the spatial correlation kernel should be considered as a more general kernel. Indeed, the fully spatially correlated interferece that the wave function kernel models, is a particular case of modeling for the spatial correlation kernel.

5. Some illustrative examples

Optical and quantum interference modelling at the micro and nano-scales, based on the two-point correlation and the reduced kernel, is illustrated with some examples.

A mask with a nano-structured hexagon honeycomb opening for optical interference is considered in figure 7. Uniform illumination and maximal spatial correlation is assumed. The nano-structured opening is composed by 10 identical thin hexagon profiles covering an area of $4\lambda \times 4\lambda$, as shown in (a). It encloses 45 (blue dots) vertices of $\mathbf{w}_{MD}^{(R)}(\xi_A; \mathbf{r}_A)$-cones, placed at the hexagon vertices and the midpoint of their largest sides. The red dots represent the vertices of $\mathbf{w}_{MD}^{(V)}(\xi_A; \mathbf{r}_A)$-cones. The power spectrum of the interference patterns described by equation (15) are shown in pseudo-color in order to improve the details, near the mask in (b) and far away from the mask in (c). It is worth noting that the pattern in (c) resembles the diffraction pattern produced by a circular opening, known as Airy pattern [11]. It is due to the approximated rotation-symmetry of the nano-structured contour and the distribution of the blue dots in the opening, in such a way that the separation of any consecutive pair of blue dots is shorter than λ [17].

This example suggests the application of the proposed model to accurately simulate the recently reported experiments on particle diffraction through graphene lattices [18].

The nano-structured mask in figure 8(a) is composed by a central hole and two concentric thin rings with diameter 4λ for the outer ring. The uniform distribution of blue dots represents the vertices of $\mathbf{w}_{MD}^{(R)}(\xi_A; \mathbf{r}_A)$-cones contained in the ring openings. The red dots represent the vertices of $\mathbf{w}_{MD}^{(V)}(\xi_A; \mathbf{r}_A)$-cones. Uniform illumination of the nano-structured mask and full spatial correlation is assumed.

The *rms*-descriptor in figure 8(b) compares the morphology of the patterns produced by the masks in figures 7(a) and 8(a), which are described by equation (15), along the z-axis. The profile tends asymptotically to null thus pointing out that the patterns become closely similar as the propagation distance increases. Indeed, the pattern morphologies are similar in more than 95% for $z \geqslant 5\lambda$. This result stresses the relevance of the symmetries in the design of nano-structured masks for photonic applications.

It is specially appreciated in the optical interference modelling by using elaborated nano-structured masks, as illustrated in figure 9(a). The mask has a snowflake nano-structured

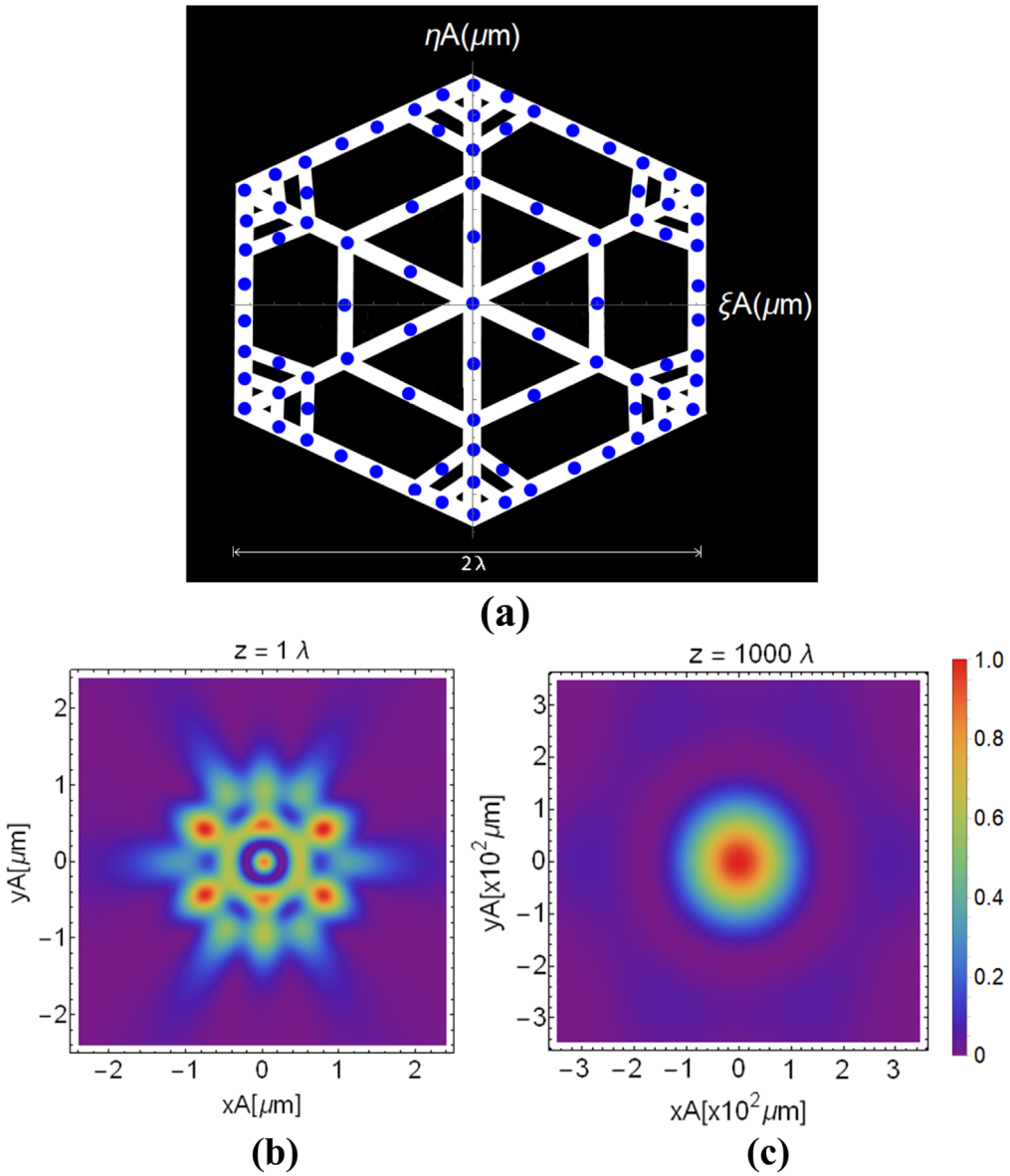

Figure 9. (a) Snowflake nano-structured mask for optical interference ($\lambda = 0.632\ \mu$m), with main diagonal length 2λ. The mask opening contains 85 uniformly distributed vertices of $\mathbf{w}_{MD}^{(R)}(\xi_A;\ \mathbf{r}_A)$-cones (blue dots). Uniform illumination of the mask under full spatial correlation is assumed. The vertices of $\mathbf{w}_{MD}^{(V)}(\xi_A;\ \mathbf{r}_A)$-cones are omitted for illustration purposes. Diffracted light produces the patterns described by equation (15), near the mask ($z = \lambda$) in (b) and far away from the mask ($z = 1000\lambda$) in (c). The patterns are presented in pseudo-color for enhancing the morphological details.

opening, whose main diagonal length is 2λ. 85 vertices of $\mathbf{w}_{MD}^{(R)}(\xi_A;\ \mathbf{r}_A)$-cones distribute uniformly along the opening contours, and uniform illumination under full spatial correlation is assumed.

The morphologies of the power spectrum patterns near the mask in figures 7(b) and 9(b) are clearly different, but they become similar far away from the mask, as shown by graphs 7 (c) and 9 (c). Results in figure 9 illustrate the capability of the 3D non-paraxial reduced kernel to model accurately optical interference produced by exotic nano-structures.

Figure 10 illustrates the simulation of the Fresnel diffraction pattern produced by single electron interference [19]. Electrons prepared with de Broglie wavelength $\lambda = 4$ pm cross a circular opening of radius 3λ, and the pattern build-up is simulated at $z = 3\lambda$ by accumulating electron arrivals at each detector pixel. An ideal detector with pixels of size 0.04 pm was modeled. The counts of electron arrivals at each pixel are shown on the colored bar on the right side of each graph and the red dot in the graph represents the last single electron arrival.

The pattern has circular symmetry as expected, and exhibits a local minimun at its center. Altought the size of the

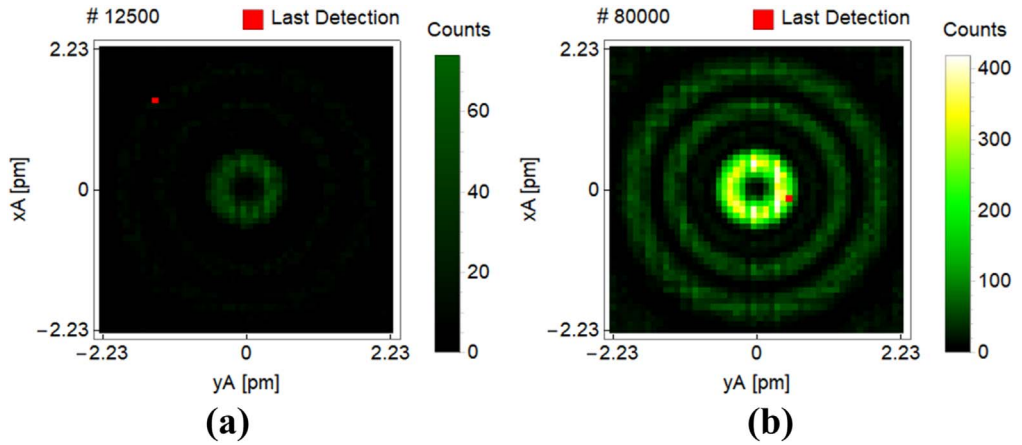

Figure 10. Build-up of the Fresnel diffraction pattern by single electrons with de Broglie wavelength of $\lambda = 4pm$. Electrons cross a circular opening of radius 3λ, under full spatial correlation and the pattern is simulated at $z = 3\lambda$. Graph (a) shows the pattern after 12500 electron arrivals, and graph (b) shows the pattern after 80000 arrivals.

diffracion mask and the detector, as well as the propagation distance are yet not achievable by the current technology, this example clearly illustrates the capability of the reduced kernel to model the behavior of single particles in quantum interference, very near from the mask. It also stresses the pertinence of the spatial correlation based modelling of optical and quantum interference at the micro and nano-scales.

6. Conclusions

Optical and quantum interference at the micro and nano-scales were described in terms of the modal expansion of the non-local function $w_M(\xi_+, \xi_-)$ on the same 3D non-paraxial geometric kernel. This kernel was rigorously deduced from both the optical wave equation for free-space propagation and the Schrödinger equation for field-free propagation, and its geometrical interpretation offers a unified framework to describe the spatial features of optical and quantum interference. It was shown that non-locality at the input plane is a necessary condition for interference, which results from a spatial modulation described by the kernel. This condition is established in the framework of the spatial (two-point) correlation and accounts for individual experimental realizations as well as for the experimental outcomes after a significant number of individual realizations. Because the kernel is essentially determined by the boundary conditions imposed by the setup, the model gives a central role to the experimental arrangement in the interference of waves and particles.

The kernel is composed by terms of different decay rates along the propagation axis, and it was showed that the term with the slowest decay can be considered as exact for $z \geqslant \lambda/2$ while for $z < \lambda/2$ it provides a relatively small departure in the outcome values. This criterion was discussed for different boundary conditions and experimental parameters. Therefore, the reduced kernel can be used to describe optical and quantum interference at the micro and nano-scales, as well as to predict accurately the experimental outcomes of both individual realizations and whole experiments with a significant number of individual realizations. Furthermore, the same kernel can be used for diffraction by appropriately shortening the spacing of cone vertices distributed on the input plane.

Examples of non-paraxial optical and quantum interference modeling with the reduced 3D kernel and by considering nano-structured masks were discussed, and the capability of the kernel to describe the behavior very near from the mask was stressed.

To our knowledge, this kernel and its geometric analysis is proposed for the first time for single particle quantum interference and its application to optical interference at the micro and nano-scales is a novelty too.

Acknowledgments

This research was supported by Universidad Nacional de Colombia, project with Hermes Code 43345. Román Castañeda is very grateful to Giorgio Matteucci for the inspiring discussions.

Author contributions

Authors contributed equally to the discussion of the subject and the paper preparation.

Competing interests

Authors declare no competing interests.

Appendix A. The helmholtz-kirchhoff integral theorem

Let us consider the volume V contained in a closed surface S and a continuous and differentiable vector field $\mathbf{A}$, defined in

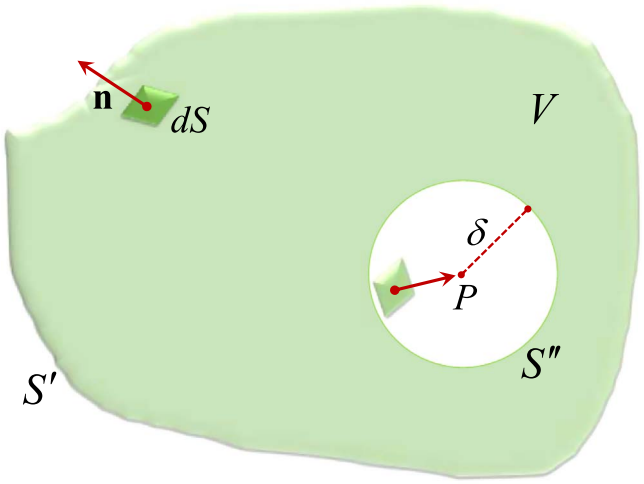

Figure A1. Conceptual sketch of the integration domain for the Green´s theorem in equation (A1).

that volume and its surface. It must fulfil the divergence theorem $\int_V \nabla \cdot \mathbf{A} dV = \oint_S \mathbf{A} \cdot d\mathbf{S}$. Let us define the vector field as $\mathbf{A} = G\nabla\psi - \psi\nabla G$, with ψ the eigen-function of equation (3) to be determined, and G a further eigen-function of equation (3) called the Green's function of the system [20]. Accordingly, $\nabla \cdot \mathbf{A} = G\nabla^2\psi - \psi\nabla^2 G = 0$ holds, and the divergence theorem yields the Green's theorem [20],

$$\oint_S (G\nabla\psi - \psi\nabla G) \cdot d\mathbf{S} = \oint_S \left(G\frac{\partial\psi}{\partial n} - \psi\frac{\partial G}{\partial n} \right) dS = 0, \tag{A1}$$

with $\partial/\partial n$ the derivative along the normal to the integration surface. The Green's theorem determines the value $\psi(P)$ at the point P in the volume enclosed by its integration surface, by isolating it into a sphere of arbitrary small radius δ, centered at P, as conceptually sketched in figure A1. It is the simplest isolating volume compatible with the isotropic swept of the integration surface from P. Therefore, the integration surface in equation (A1) can be expressed as $S \equiv \lim_{\delta \to 0} \{S' \bigcup S''\}$.

takes the form

$$\lim_{\delta \to 0} \delta^2 \oint_{S''} \left(\frac{\partial\psi}{\partial n} - \psi\left(ik - \frac{1}{\delta} \right) \right) \frac{\exp(ik\delta)}{\delta} d\Omega$$
$$= \lim_{\delta \to 0} 4\pi \ \delta^2 \left(\frac{\partial\psi(P)}{\partial n} - \psi(P)\left(ik - \frac{1}{\delta} \right) \right),$$
$$\times \frac{\exp(ik\delta)}{\delta} = -4\pi \ \psi(P)$$

where $dS = \delta^2 d\Omega$, with $d\Omega$ the differential solid angle that subtends the differential surface on S'' from P. Furthermore, $S' \to S$ as $\delta \to 0$. Consequently, equation (A1) yields

$$\psi(P) = \frac{1}{4\pi} \oint_S \left(\frac{\partial\psi}{\partial n} \frac{\exp(ik|\mathbf{r}|)}{|\mathbf{r}|} - \psi \frac{\partial}{\partial n} \left(\frac{\exp(ik|\mathbf{r}|)}{|\mathbf{r}|} \right) \right) dS, \tag{A2}$$

which is known as the Helmholtz-Kirchhoff integral theorem [20]. It gives the values of the eigen-function ψ at any point in the volume enclosed by the integration surface in terms of a modal expansion, whose kernel is determined by the Green's function of the system and its derivative, while the coefficients are the values of ψ and its derivative on the integration surface, i.e. on the considered boundary condition.

It should be stressed that the kernel modes are scalar, geometric and deterministic functions, defined in the volume, which connect the point P with the integration surface. Therefore, they must be compatible with the specific boundary conditions imposed to equation (3).

Appendix B. Preparation of the non-local function

Let us consider the arrangement of the additional stage in figure B1, preceding the setup in figure 2. The preparation of the nonlocal function $w_M(\xi_+, \xi_-)$ can be described by applying the Helmholtz-Kirchhoff integral theorem, too.

To this aim, the S plane is included in the boundary conditions and the M plane is within the volume delimited by the integration surface in figure 1. Thus the eigen-function at the M plane can be expressed as

$$\psi_M(\xi) = -i\frac{k}{4\pi} \int_S d^2r' \ \psi_S(\mathbf{r}') \left(\frac{z' + |\mathbf{z}' + \boldsymbol{\xi} - \mathbf{r}'|}{|\mathbf{z}' + \boldsymbol{\xi} - \mathbf{r}'|^2} \right) \exp(ik \ |\mathbf{z}' + \boldsymbol{\xi} - \mathbf{r}'|)$$
$$+ \frac{1}{4\pi} \int_S d^2r' \ \psi_S(\mathbf{r}') \left(\frac{z'}{|\mathbf{z}' + \boldsymbol{\xi} - \mathbf{r}'|^3} \right) \exp(ik \ |\mathbf{z}' + \boldsymbol{\xi} - \mathbf{r}'|). \tag{B1}$$

The most suitable mathematical form of the Green's function for this boundary condition should have spherical symmetry, i.e. $G(\mathbf{r}) = \exp(ik|\mathbf{r}|)/|\mathbf{r}|$, with $|\mathbf{r}|$ the distance from P to any arbitrary point Q on the integration surface. Indeed, $G(\mathbf{r}) = \frac{\exp(ik\delta)}{\delta}$ and $\frac{\partial G}{\partial n} = \left(ik - \frac{1}{\delta} \right) \frac{\exp(ik\delta)}{\delta}$ on S'', so that the component of equation (A1) on this surface and similarly interpreted as equation (6). So, the nonlocal function $w_M(\xi_+, \xi_-)$ straightforwardly results from multiplying equation (B1) by its complex conjugate at two points (ξ_+, ξ_-). It can be denoted as

$$w_M(\boldsymbol{\xi}_+, \boldsymbol{\xi}_-) = \int_S d^2r'_A \ \mathbf{w}_{SM}(\mathbf{r}'_A; \boldsymbol{\xi}_+, \boldsymbol{\xi}_-; \mathbf{z}', k). \tag{B2}$$

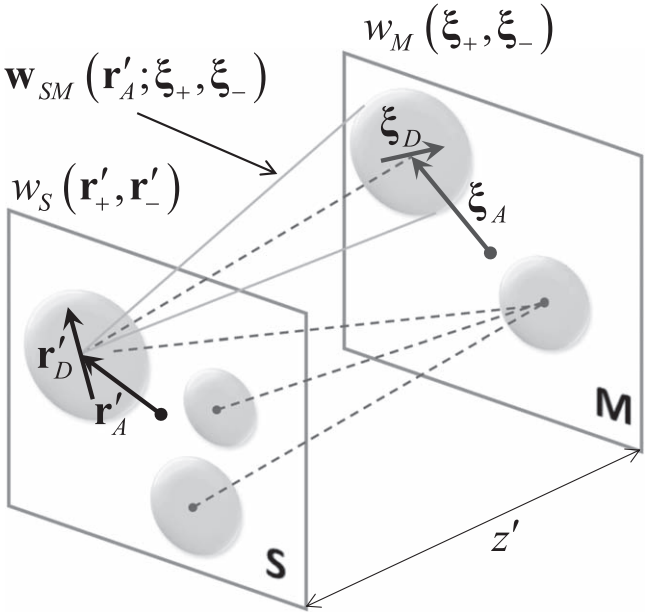

Figure B1. Conceptual sketch for the preparation of the nonlocal function $w_M(\xi_+, \xi_-)$. Reduced coordinates are depicted by the arrows on the planes. The shadowed circles represent the regions around given points $\mathbf{r}'_A$ on the S plane and ξ_A on the M plane where the nonlocal functions $w_S(\mathbf{r}'_+, \mathbf{r}'_-)$ and $w_M(\xi_+, \xi_-)$ takes on non-null values, respectively.

Therefore, $w_M(\xi_+, \xi_-)$ is the cross-section at the M plane of overlapped cones $\mathbf{w}_{SM}(\mathbf{r}'_A; \xi_+, \xi_-; \mathbf{z}', k)$ with vertices at the emitting points $\mathbf{r}'_A$ on the S plane and the same basis, centered at a given point ξ_A, that is the midpoint of the pairs for which $w_M(\xi_+, \xi_-)$ takes on non-null values.

For similar reasons as those in the analysis of equation (14), these cones can be expressed as

$$\mathbf{w}_{SM}(\mathbf{r}'_A; \boldsymbol{\xi}_+, \boldsymbol{\xi}_-; \mathbf{z}', k) = \mathbf{w}^{(R)}_{SM}(\mathbf{r}'_A; \xi_+, \xi_-; \mathbf{z}', k) + \mathbf{w}^{(V)}_{SM}(\mathbf{r}'_A; \xi_+, \xi_-; \mathbf{z}', k), \tag{B3}$$

with

$$\mathbf{w}^{(R)}_{SM}(\mathbf{r}'_A; \xi_+, \xi_-; \mathbf{z}', k) = |\psi_S(\mathbf{r}'_A)|^2 \ \Phi_{SM}(\mathbf{r}'_A; \xi_+, \xi_-; \mathbf{z}', k), \tag{B4}$$

the cone component contributed by the local values $w_S(\mathbf{r}'_A, \mathbf{r}'_A) = |\psi_S(\mathbf{r}'_A)|^2$ at the S plane, and

$$\mathbf{w}^{(V)}_{SM}(\mathbf{r}'_A; \xi_+, \xi_-; \mathbf{z}', k) = \int_{\substack{S \\ \mathbf{r}'_D \neq 0}} d^2r'_D \ w_S(\mathbf{r}'_+, \mathbf{r}'_-) \Phi_{SM}(\mathbf{r}'_+, \mathbf{r}'_-; \xi_+, \xi_-; \mathbf{z}', k), \tag{B5}$$

the cone component contributed by the nonlocal function $w_S(\mathbf{r}'_+, \mathbf{r}'_-) = \psi_S(\mathbf{r}'_+) \ \psi^*_S(\mathbf{r}'_-)$ centered at the emitting point $\mathbf{r}'_A$ on the S plane. So, the integration domain of equation (B5) is the emitting region around the point $\mathbf{r}'_A$ that is the midpoint of the pairs at which the nonlocal function $w_S(\mathbf{r}'_+, \mathbf{r}'_-)$ takes non-null values. The kernel of the modal expansion in equation (B5) is given by the 3D non-paraxial modes in the volume between the S and the M planes

$$\begin{aligned}\Phi_{SM}(\mathbf{r}'_+, \mathbf{r}'_-; \xi_+, \xi_-; \mathbf{z}', k) &= \frac{1}{(4\pi)^2}\Bigg[k^2 \left(\frac{z' + |\mathbf{z}' + \xi_+ - \mathbf{r}'_+|}{|\mathbf{z}' + \xi_+ - \mathbf{r}'_+|^2}\right)\left(\frac{z' + |\mathbf{z}' + \xi_- - \mathbf{r}'_-|}{|\mathbf{z}' + \xi_- - \mathbf{r}'_-|^2}\right) \\ &+ ik\left(\frac{z'}{|\mathbf{z}' + \xi_+ - \mathbf{r}'_+|^3}\right)\left(\frac{z' + |\mathbf{z}' + \xi_- - \mathbf{r}'_-|}{|\mathbf{z}' + \xi_- - \mathbf{r}'_-|^2}\right) \\ &- ik\left(\frac{z' + |\mathbf{z}' + \xi_+ - \mathbf{r}'_+|}{|\mathbf{z}' + \xi_+ - \mathbf{r}'_+|^2}\right)\left(\frac{z'}{|\mathbf{z}' + \xi_- - \mathbf{r}'_-|^3}\right) \\ &+ \left(\frac{z'}{|\mathbf{z}' + \xi_+ - \mathbf{r}'_+|^3}\right)\left(\frac{z'}{|\mathbf{z}' + \xi_- - \mathbf{r}'_-|^3}\right)\Bigg] \\ &\exp(ik\,|\mathbf{z}' + \xi_+ - \mathbf{r}'_+| - ik\,|\mathbf{z}' + \xi_- - \mathbf{r}'_-|),\end{aligned} \tag{B6}$$

and the kernel in equation (B4) is obtained by locally evaluating equation (B6) at the S plane, i.e. for $\mathbf{r}'_D = 0$. Therefore, the prepared non-local function at the M plane can be expressed as

$$w_M(\xi_+, \xi_-) = w^{(R)}_M(\xi_+, \xi_-) + w^{(V)}_M(\xi_+, \xi_-), \tag{B7}$$

whose terms are obtained by respectively replacing equations (B4) and (B5) in equation (B2). Thus, the component

$$w^{(R)}_R(\xi_+, \xi_-) = \int_S d^2r'_A \ \ |\psi_S(\mathbf{r}'_A)|^2 \ \ \Phi_{SM}(\mathbf{r}'_A; \xi_+, \xi_-; \mathbf{z}', k), \tag{B8}$$

is contributed by the local values $w_S(\mathbf{r}'_A, \mathbf{r}'_A)$ at the S plane, while the non-local values of $w_S(\mathbf{r}'_+, \mathbf{r}'_-)$ for $\mathbf{r}'_D \neq 0$ contribute the component $w^{(V)}_M(\xi_+, \xi_-)$. This result underlines the role of the 3D non-paraxial geometric modes $\Phi_{SM}(\mathbf{r}'_+, \mathbf{r}'_-; \xi_+, \xi_-; \mathbf{z}', k)$ in the determination of the prepared nonlocal function $w_M(\boldsymbol{\xi}_+, \boldsymbol{\xi}_-)$. Specifically, equation (B8) points out that non-locality at the S plane is not a necessary condition to prepare $w_M(\boldsymbol{\xi}_+, \boldsymbol{\xi}_-)$. It means that $w_M(\xi_+, \xi_-)$ has a fundamental geometric meaning on account of the modes $\Phi_{SM}(\mathbf{r}'_+, \mathbf{r}'_-; \xi_+, \xi_-; \mathbf{z}', k)$, which are essentially determined by the boundary conditions at the S plane. This geometric meaning is not altered by the non-locality of the component $w^{(V)}_M(\xi_+, \xi_-)$, which should be taken into account if the effective source of waves or particles attached at the S plane is spatially correlated. In this case, the corresponding modes, also determined by the boundary conditions, are selected by such correlation properties, i.e. $w_S(\mathbf{r}'_+, \mathbf{r}'_-)$ behaves like a modal filter [13, 14].

ORCID iDs

Román Castañeda https://orcid.org/0000-0002-1805-3958
Jaime Moreno https://orcid.org/0000-0001-5947-2932
Daniel Colorado https://orcid.org/0000-0002-8585-4034
Julián Laverde https://orcid.org/0000-0002-4403-390X

References

[1] Mandel L and Wolf E 1995 *Optical Coherence and Quantum Optics* (Cambridge: Cambridge University Press)
[2] Castañeda R and Moreno J 2019 Three-dimensional nonparaxial characterization of physical point sources *J. Opt. Soc. Am.* A **36** 1657–62

[3] Feynman R, Leighton R and Sands M 1965 *The Feynman Lectures on Physics* (Menlo Park: Addison–Wesley) vol 3
[4] Feynman R and Hibbs A 1965 *Quantum Mechanics and Path Integrals* (New York: McGraw-Hill)
[5] Robichaux M A, Potter L, Zhang Z, He F, Liu J, Schmid M F and Wensel T G 2019 *Defining the Layers of a Sensory Cilium with STORM and Cryo-Electron Nanoscopy PNAS* 23562–72 https://ssrn.com/abstract=3155933
[6] Brand C, Debiossac M, Susi T, Aguillon F, Kotakoski J, Roncin P and Arndt M 2019 Coherent diffraction of hydrogen through the 246 pm lattice of graphene *New J. Phys.* **21** 033004 Accepted
[7] Li Z Y 2019 Atom interferometers with weak-measurement path detectors and their quantum mechanical analysis *Chin. Phys.* B **28** 060301 (21 pages)
[8] Vieira C H S, Costa H A S, de Souza G, Sampaio M and da Paz I G 2019 Fringe visibility of exotic trajectories for matter waves in a double-slit experiment *Mod. Phys. Let.* A **34** 1950233 (15 pages)
[9] Kocsis S, Braverman B, Ravets S, Stevens M J, Mirin R P, Shalm L K and Steinberg A M 2011 Observing the Average Trajectories of Single Photons in a Two-Slit Interferometer *Science* **332** 1170–3
[10] Catañeda R, Laverde J and Moreno J 2020 Matrix algorithm for 3D nonparaxial optical field modeling under arbitrary spatial coherence *Appl. Opt.* **59** D21–30
[11] Born M and Wolf E 1993 *Principles of Optics* 6th edn (Oxford: Pergamon)
[12] Van Boxem R, Partoens B and Verbeeck J 2013 Dirac Kirchhoff diffraction theory ArXiv1303.0954v1 [quant-ph] 5 Mar
[13] Castañeda R 2017 Interaction description of light propagation *J. Opt. Soc. Am.* A **34** 1035–44
[14] Castañeda R and Matteucci G 2017 New physical principle for interference of light and material particles *Advances in Imaging and Electron Physics* ed P W Hawkes (AP: Elsevier) vol 204, p 1
[15] de Martini F, Denardo G and Zeilinger A 1993 *Proc. of the Adriatico Worshop on Quantum Interferometry* (Singapore: World Scientific)
[16] Glauber R J 1963 The quantum theory of optical coherence *Phys. Rev.* **130** 2529–39
[17] Castañeda R 2017 Discreteness of the real point emitters as a physical condition for diffraction *J. Opt. Soc. Am.* A **34** 184–92
[18] Zhao W *et al* 2017 Low-energy transmission electron diffraction and imaging of large-area graphene *Sci. Adv.* **3** e1603231 (8 pages)
[19] Matteucci G 1990 Electron wavelike behavior: a historical and experimental introduction *Am. J. Phys.* **58** 1143–7
[20] Arfken G 1970 *Mathematical Methods for Physicists* 2nd edn (New York: Academic)